POLITECNICO DI TORINO
Repository ISTITUZIONALE

Fast Determination of Feasible Torque-Speed Range for Variable Flux Machines Including Remagnetization Voltage Limit

Original
Fast Determination of Feasible Torque-Speed Range for Variable Flux Machines Including Remagnetization Voltage Limit / Chen, C., Pescetto, P., Ferrari, S., Olson, G.F., Diana, M., Thiringer, T., Pellegrino, G.. - (2025), pp. 1-8. (2025 IEEE Energy Conversion Conference Congress and Exposition (ECCE)) [10.1109/ecce58356.2025.11260140].

Availability:
This version is available at: 11583/3007093 since: 2026-01-29T15:47:17Z

Publisher:
IEEE

Published
DOI:10.1109/ecce58356.2025.11260140

Terms of use:

This article is made available under terms and conditions as specified in the corresponding bibliographic description in the repository

Publisher copyright
IEEE postprint/Author's Accepted Manuscript

©2025 IEEE. Personal use of this material is permitted. Permission from IEEE must be obtained for all other uses, in any current or future media, including reprinting/republishing this material for advertising or promotional purposes, creating new collecting works, for resale or lists, or reuse of any copyrighted component of this work in other works.

(Article begins on next page)

10 August 2026

Fast Determination of Feasible Torque-Speed Range for Variable Flux Machines Including Remagnetization Voltage Limit

Chen Chen
Energy Dep. Galileo Ferraris
Politecnico di Torino
Torino, Italy
chen_chen@polito.it

Paolo Pescetto
Energy Dep. Galileo Ferraris
Politecnico di Torino
Torino, Italy
paolo.pescetto@polito.it

Simone Ferrari
Energy Dep. Galileo Ferraris
Politecnico di Torino
Torino, Italy
simone.ferrari@polito.it

Gustaf Falk Olson
Electric Driveline Department
Volvo Cars
Göteborg, Sweden
gustaf.falk.olson@volvocars.com

Michela Diana
Electric Driveline Department
Volvo Cars
Göteborg, Sweden
michela.diana@volvocars.com

Torbjörn Thiringer
Dep. of Electrical Engineering
Chalmers University of Technology
Göteborg, Sweden
torbjorn.thiringer@chalmers.se

Gianmario Pellegrino
Energy Dep. Galileo Ferraris
Politecnico di Torino
Torino, Italy
gianmario.pellegrino@polito.it

***Abstract*—This paper presents a computationally efficient method for determining the feasible operating range of Variable-Flux Machines (VFMs) under inverter voltage constraints. Remagnetization transients in VFMs demand substantial current and armature flux, resulting in elevated voltage requirements and pronounced speed limitations. To address this, the proposed approach leverages precomputed Finite Element Analysis (FEA) flux and magnetization maps to define torque–speed boundaries under voltage-limited conditions while considering the high voltage demand during remagnetization, eliminating the need for iterative field simulations or FEA co-simulation. The method is validated through driving cycle simulations, demonstrating the reduction in available traction and braking torque due to the inability to re-magnetize the machine beyond the voltage-speed limit. The results provide key insights for optimizing magnetization state control and mission profile planning in traction applications using VFMs.**

***Index Terms*—Variable Flux Machines, Memory Motors, Voltage Limitation, Re-Magnetization, Torque-speed profile, Driving Cycles, Load Profile.**

I. Introduction

Permanent Magnet Synchronous Motors (PMSMs) are widely adopted in high-performance traction motors, thanks to their high efficiency and power density [1]–[5]. However, the supply chain instability and environmental cost of the rare-earth magnets, particularly NdFeB magnets, are leading the search for alternative solutions that do not rely on rare-earth magnets [6]–[8]. One of the potential candidates is Variable-Flux Machines (VFMs) [9], also known as memory motors.

The VFMs utilize low-coercivity permanent magnets (PMs) to allow PM flux regulation [10]–[12]. This process is also called Magnetization State (MS) manipulation, performed by injecting magnetization or demagnetization current pulses in specific directions of the dq plane. This permits achieving improved efficiency and extended speed region compared to conventional Neodymium-based PMSMs [13]–[16]. In particular, a high MS is desirable at standstill and in the low speed range, to obtain high torque ratings. When targeting higher speed, so inverter voltage limitation is reached, effective field weakening is achieved by reducing the MS, i.e. partially demagnetizing the low coercivity PMs. The feasible operating area of VFMs is often considered as the envelop of maximum torque Vs speed profile associated with each MS [17]–[20].

The MS manipulation can be performed at zero load and speed for washing machine application [21]–[23]. However, interrupting torque is required before applying magnetization or demagnetization processes, and it is not realistic for traction applications. Performing MS manipulation without stopping motor is challenging, as inverter current and voltage limits bring critical constraints. The re-magnetization transients is particularly critical, as a large current pulse is required. Such high current pulse significantly increases the flux linkage of the motor, easily saturating the available inverter voltage at non-zero speed. While existing strategies address loaded operation [11], [24], they do not explicitly account for voltage constraints during remagnetization transients, which can significantly restrict feasible operating areas with respect to the maximum torque Vs speed envelop at different MS. This is often evaluated by means of finite element analysis (FEA) based simulations which are highly computational intensive, requiring significant simulation time and storage demand.

To cover this lack, this paper proposes a novel method for determining feasible operating areas under inverter voltage constraints, including the remagnetization transients. Unlike FEA-based approaches, the proposed method entirely relies on the manipulation of pre-calculated flux maps and magnetization maps. The method, validated on a full-scale vehicle across two simulated driving cycles, enables the rapid and accurate

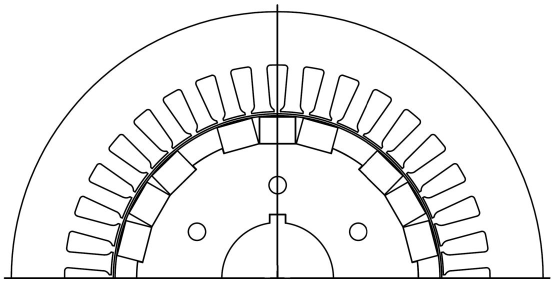

Fig. 1: Cross-section of the VFM prototype under test.

TABLE I: Motor data

DC-link voltage	600 V
Maximum torque current	25 A
Maximum torque at MS 80%	35 Nm
Base speed at MS 80%	2600 rpm
Motor maximum speed	12000 rpm
Remag current	70 A
Nominal flux linkage	0.374 Vs

evaluation of the remagnetization voltage limit in the torque-speed domain and permits the optimization of the MS control strategy for any vehicle mission.

II. Motor Under Test and VFM Model

The Machine Under Test (MUT) is a 3-pole-pair VFM Surface-mounted PM (SPM) machine equipped with AlNiCo5 magnets and a carbon fiber sleeve for rotor structural integrity. The geometry is shown in Fig. 1 and its ratings are listed in Table I. This machine was in-house designed as a down-scaled proof-of-concept traction motor for hybrid and full electric vehicles. A prototype of this machine is currently being manufactured. The MS of VFMs is defined as:

$$MS = \frac{\lambda_m}{\lambda_{m,max}} \tag{1}$$

where λ_m is the PM flux linkage and $\lambda_{m,max}$ corresponds to 100% magnetization. The motor voltage equation is expressed in the dq rotating reference frame:

$$\boldsymbol{v}_{dq} = R_s \boldsymbol{i}_{dq} + \frac{d\boldsymbol{\lambda}_{dq}}{dt} + \omega \boldsymbol{J} \boldsymbol{\lambda}_{dq} \tag{2}$$

where bold symbols indicate a vector notation, R_s is the stator resistance, $\boldsymbol{v}_{dq}$, $\boldsymbol{i}_{dq}$ and $\boldsymbol{\lambda}_{dq}$ are the stator voltage, current and flux vectors, ω is the electrical pulsation and $\boldsymbol{J} = \begin{bmatrix} 0 & -1 \\ 1 & 0 \end{bmatrix}$ is the imaginary unit expressed in matrix form.

Due to magnetic saturation and cross-saturation phenomena, the flux linkage is a nonlinear function of both current components, over the MS:

$$\begin{cases} \lambda_d = \lambda_d\left(i_d, i_q, MS\right) \\ \lambda_q = \lambda_q\left(i_d, i_q, MS\right) \end{cases} \tag{3}$$

Such nonlinear characteristics, often called flux maps, can either be computed through FEA simulations or measured in experiments. The flux maps of the MUT are shown in Figs. 2a and 2b, omitting cross-saturation for ease of visualization. The steady-state $T-n$ profiles at $V_{dc}=600$V and $I_{max}=25$A are depicted in Fig. 2c for different MS values between 40% and 80%. Any MS value lower than 40% is not considered, as it does not produce significant torque or speed advantages. Conversely, MS >80% is avoided as it is prone to undesired demagnetization.

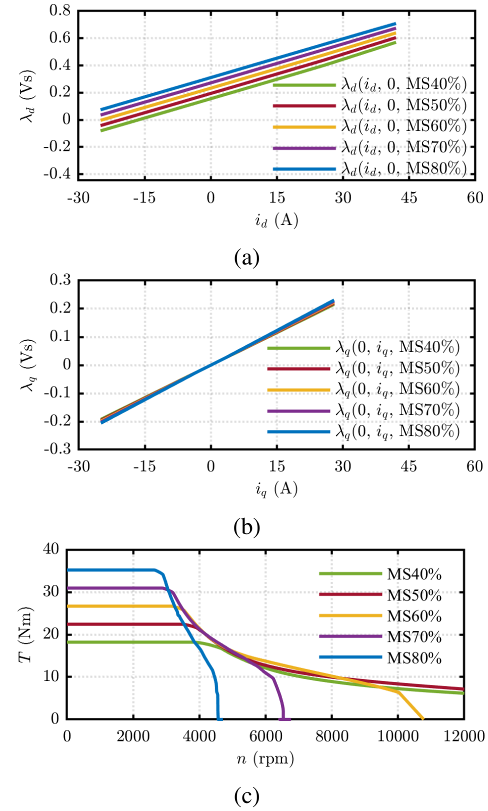

Fig. 2: FEA calculated maps for different MSs, (a) λ_d map, (b) λ_q map and (c) $T-n$ profiles.

A. Demag and Remag Maps

In VFMs, the MS variation is performed by imposing current pulses in the dq plane. The amplitude and direction of the current pulse required to achieve the target MS can be represented in the Demag and Remag maps [25], reported in Fig. 3. Starting with a fully magnetized machine ($MS=100\%$), the Demag map indicates the MS achieved after a demagnetization current pulse in the second quadrant of the dq plane. Similarily, the Remag map reports the MS achieved for any remagnetization current pulse in the first quadrant while starting from $MS=0$. Detailed procedures to obtain these maps are available in [25], [26].

As an example of the demagnetization process, if the motor operates at high MS (e.g. 80%), a dq-current pulse of i_d=-17 A and i_q=8 A demagnetizes the machine to MS=50% according to Fig. 3a. Similarly, if the VFM operates at low MS (e.g. 20%), a current pulse i_d=70 A, i_q=17 A remagnetizes the VFM to MS=80% based on Fig. 3b.

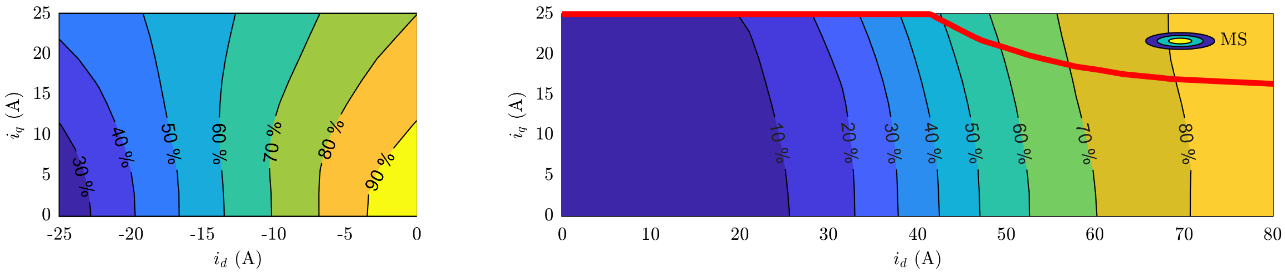

(a) (b)

Fig. 3: MS characteristics of the MUT. (a) Demag map. (b) Remag map; the red curve represents the current trajectory for obtaining constant T= 19 Nm.

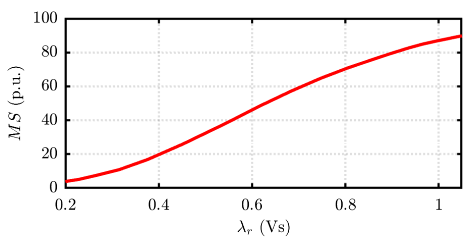

Fig. 4: λ_r vs MS re-magnetization characteristic.

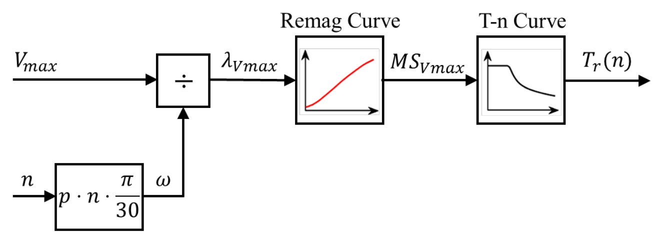

Fig. 5: Block diagram depicting the calculation of the re-magnetization voltage limit curve.

B. Demag and Remag Under Load

Combining the Demag and Remag maps with flux maps represented in Figs. 2a and 2b, the flux linkage generated during MS variation transition can be obtained, thus the involved electromagnetic torque can be computed.

Based on the Demag and Remag maps and the associated torque map, optimal amplitude and direction of the current pulses can be derived. In particular, the current pulse permitting to change MS under load without perturbing the controlled torque can be computed. The red line of Fig. 3b shows the current trajectory for maintaining a constant torque of 19 Nm during remagnetization.

III. RE-MAGNETIZATION VOLTAGE LIMIT

A. $MS - \lambda_r$ Remag Curve

Low-coercivity magnets allow demagnetization with relatively low current pulses; however, re-magnetization inherently requires significantly higher current, as evidenced by the Demag and Remag maps in Fig. 3. Focusing on the remagnetization characteristic, for each point of the Remag map the corresponding torque and flux linkage magnitude during the MS transition are computed using the flux maps (3). These represent the torque and flux linkage magnitude during the remagnetization current pulse, labeled T_r and λ_r respectively, where the subscript r stands for remagnetization.

The red line in Fig. 3b indicates the current pulses required to remagnetize the machine while imposing a constant torque of $T_r = 19$ Nm, i.e. the maximum torque achievable at the lowest considered $MS = 40\%$. When moving along this trajectory, the λ_r Vs MS law is obtained, called $MS - \lambda_r$ **Remag curve**, depicted in Fig. 4. Otherwise said, the $MS - \lambda_r$ Remag curve indicates the flux linkage amplitude required during the current pulse for remagnetizing the machine to a given MS while maintaining the maximum torque related to $MS = 40\%$. In order to permit PM remagnetization, such flux linkage magnitude is larger than the nominal flux (0.374 Vs), thus potentially incurring in voltage limitation.

B. Remagnetization Speed Limit under Constrained Voltage

The $MS - \lambda_r$ Remag curve can be utilized to determine the maximum speed at which the remagentization current pulse can be injected without incurring in voltage limitation. The proposed procedure is depicted in Fig. 5. When operating near the voltage limit, the machine's voltage equation (2) can be approximated as:

$$\boldsymbol{v}_{dq} \approx \omega \boldsymbol{J} \boldsymbol{\lambda}_{dq} \quad \rightarrow \quad |\boldsymbol{v}_{dq}| \approx \omega\lambda \tag{4}$$

where λ is the magnitude of $\boldsymbol{\lambda}_{dq}$. The inverter maximum voltage constraint is imposed:

$$|\boldsymbol{v}_{dq}| \leq V_{max} \tag{5}$$

Assuming a standard PWM modulation with third harmonic injection operating in the linear modulation region, $V_{max} = v_{dc}/\sqrt{3}$, where v_{dc} is the DC-link voltage.

For a given rotor test speed n, the corresponding electrical pulsation is computed:

$$\omega = n \cdot p \cdot \frac{\pi}{30} \tag{6}$$

Based on (4), the maximum flux linkage magnitude λ_{Vmax} that can be maintained at such speed is computed as:

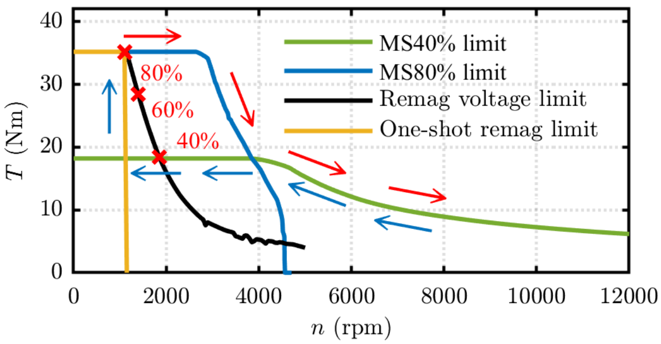

(a)

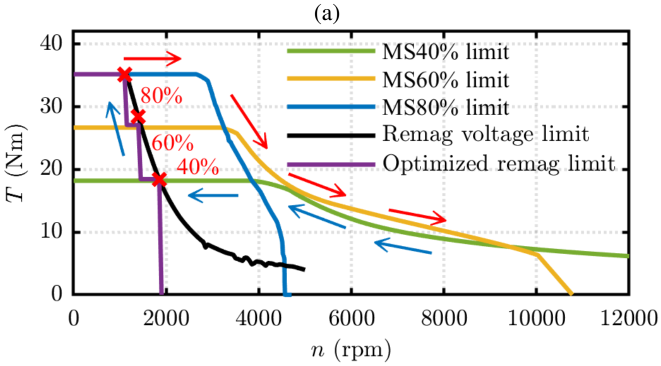

(b)

Fig. 6: VFM torque Vs speed profiles when adopting a) two MS levels, 40% and 80% (one-step re-magnetization) and b) three MS levels, 40%, 60% and 80% (two-steps re-magnetization).

$$\lambda_{Vmax} = \frac{V_{max}}{\omega} \tag{7}$$

Such flux magnitude is used as input to the MS–λ_r remagnetization curve to determine the maximum magnetization state MS_{Vmax} at which the VFM can be remagnetized at the given speed without exceeding the voltage limit. Using this MS_{Vmax} and the test speed n, the corresponding torque is obtained by interpolating the torque–speed curves shown in Fig. 2c. This yields the maximum torque T_r that can be sustained during the remagnetization transient while respecting the voltage constraint V_{max}. By repeating this procedure across a range of test speeds, a trajectory is traced in the torque–speed plane, representing the remagnetization voltage limit, shown as a solid black line in Figs. 6a and 6b.

C. Hysteresis Behavior in the Torque Vs Speed Plane

The analysis in Section III-B shows that, while the demagnetization current pulse can always be applied, the remagnetization transient is only feasible if the operating point lies to the left of the remagnetization voltage limit in the torque–speed plane, that is, if the speed is below the threshold defined by the remagnetization voltage limit trajectory. This constraint introduces a speed-dependent hysteresis in the feasible magnetization state during operation, which in turn affects the maximum achievable torque–speed profile.

For simplicity, only two magnetization states (MS = 40% and MS = 80%) are considered in Fig. 6a. The corresponding maximum torque vs. speed profiles are shown in green and blue, respectively, while the remagnetization voltage limit is indicated by the black curve. The arrows depict a simplified driving scenario: the vehicle accelerates at MS = 80%, transitions to MS = 40% for flux weakening above 4000 rpm, and then decelerates. However, due to the voltage constraint, remagnetization back to MS = 80% becomes infeasible above 1100 rpm. For visual clarity, the diagram displays the absolute torque values; during deceleration, the actual torque is negative. The yellow line highlights the speed threshold (1100 rpm) below which remagnetization to MS = 80% is possible, as dictated by the voltage limit curve.

In conclusion, the operating region between the blue and green torque profiles, and to the right of the yellow line ($n >$ 1100 rpm), is only accessible if the machine is accelerating at MS = 80% from below 1100 rpm. **This region becomes inaccessible when approaching from the flux-weakening range** at MS = 40%. This hysteresis effect, overlooked by the previous literature, imposes significant constraints on the feasible driving cycle and adversely affects drive performance. It should be highlighted that for the MUT the voltage limit occurs at relatively low speed because of the high magnitude of re-magnetization current. Demagnetization does not impose similar torque penalties, as it requires significantly less current and a flux magnitude lower than the nominal value, thus not incurring in voltage limitation.

Smaller MS steps can help mitigate the impact of the voltage limitation, as illustrated by the purple trajectory in Fig. 6b. In this example, the motor is progressively remagnetized during deceleration, first to MS = 60% at 1400 rpm, and then to MS = 80% at 1100 rpm. Reducing the MS step size further would allow the trajectory to approach the theoretical remagnetization voltage limit more closely. However, this would require more frequent injection of demagnetization and remagnetization current pulses, which may be undesirable due to increased control complexity, energy loss, or thermal impact. Therefore, a trade-off must be made between the granularity of MS variation and the severity of speed limitations imposed by the voltage constraint.

IV. Simulation Results

A. Verification of Remagnetization Voltage Limit

The accuracy of remagnetization voltage limit described in Section III-B was verified through dedicated simulations. The MUT is simulated with a high-fidelity VFM model in MATLAB/Simulink that does not require co-simulation with FEA [25]. The motor is torque controlled, while the speed is externally imposed.

In Fig. 7, a one-step remagnetization from MS = 40% to 80% is performed at a reference torque T^* = 16 Nm and speed of 1000 rpm, i.e. close to the theoretical remagnetization speed limit (black curve in Fig. 6a). A dedicated control strategy is employed, capable of injecting the demagnetization and remagnetization current pulses while maintaining constant

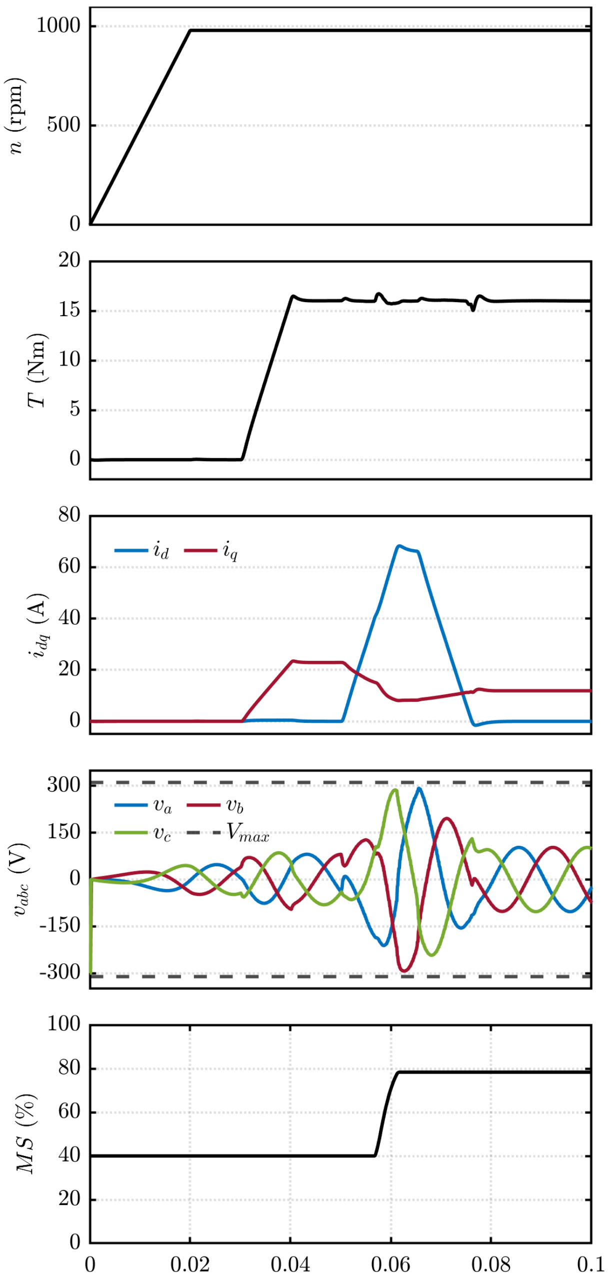

Fig. 7: Simulation results: remagnetization transient MS 40% $\rightarrow$ 80% at 1000 rpm, 16 Nm. From top to bottom: rotor speed, electromagnetic torque, stator dq-axis currents, three phase voltage with its voltage limit and MS.

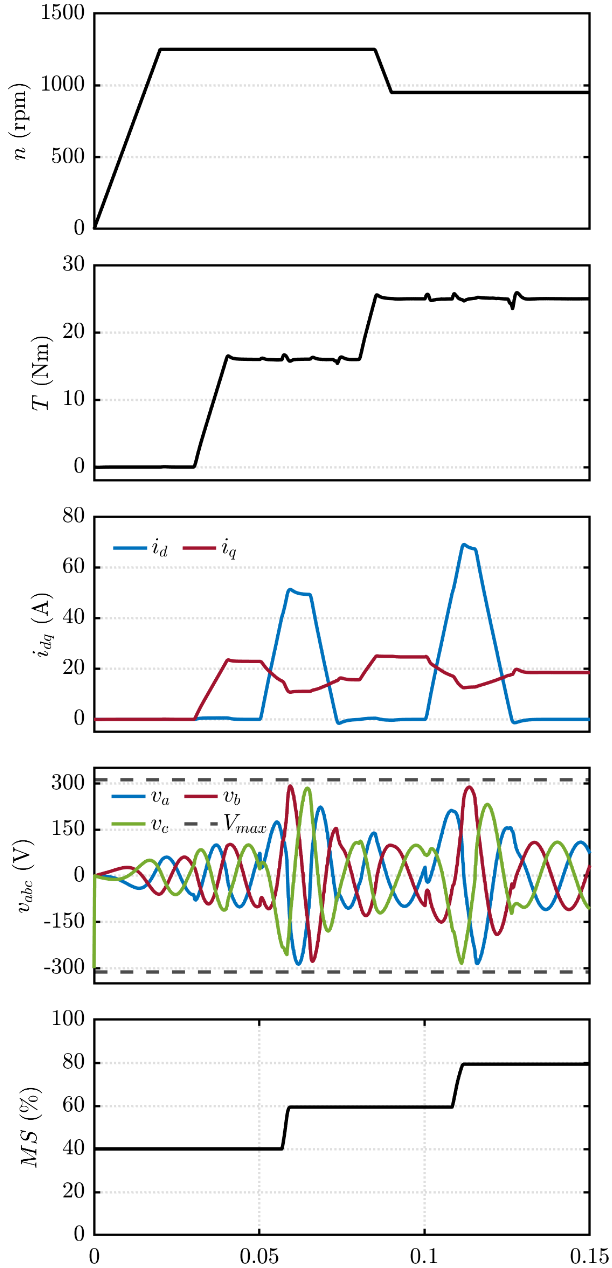

Fig. 8: Simulation results: two remagnetization transients MS 40%$\rightarrow$60% at 1300 rpm, 16 Nm and MS 60%$\rightarrow$80% at 1100 rpm, 25 Nm. From top to bottom: speed, torque, stator currents, phase voltage with its voltage limit and MS

torque control. Assuming the nominal DC-link voltage of 600 V, the voltage limit V_{max} is set to $0.9 \cdot V_{dc}/\sqrt{3}$ to account for inverter nonlinearities, resistive voltage drops, and to ensure a robust safety margin for motor control. As shown, the torque is accurately regulated throughout the remagnetization transient, while the phase voltage approaches V_{max}. This simulation confirms the validity of the remagnetization speed limit derived in Section III-B, as voltage saturation would indeed occur at higher speeds.

A second simulation is reported in Fig. 8 with a two-step remagnetization. A first remagnetization from MS 40% to 60% is imposed at 1300 rpm, 16 Nm, while the second transient from MS 60% to 80% happens at 1000 rpm, 25 Nm. Both these conditions are close to the theoretical Remag voltage limit in Fig. 6b. Both remagnetization steps generate a maximum voltage of 290 V during the MS transition, within the voltage limit V_{max} of 310 V, confirming again the accuracy of the calculated Remag voltage limit.

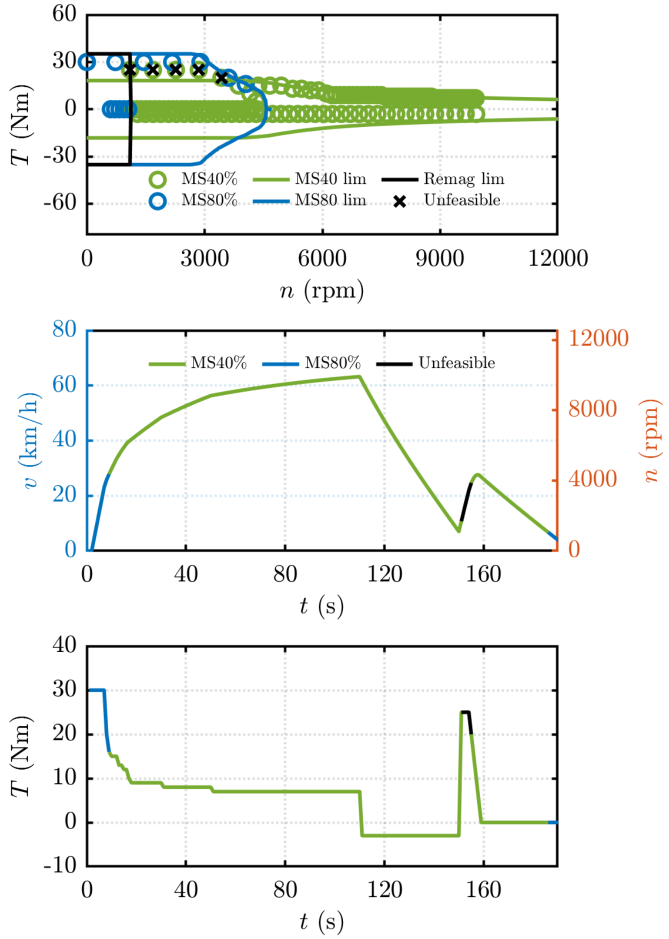

Fig. 9: Simple driving cycle test with feasible and unfeasible operating points are colored, MS switches between 40% and 80%.

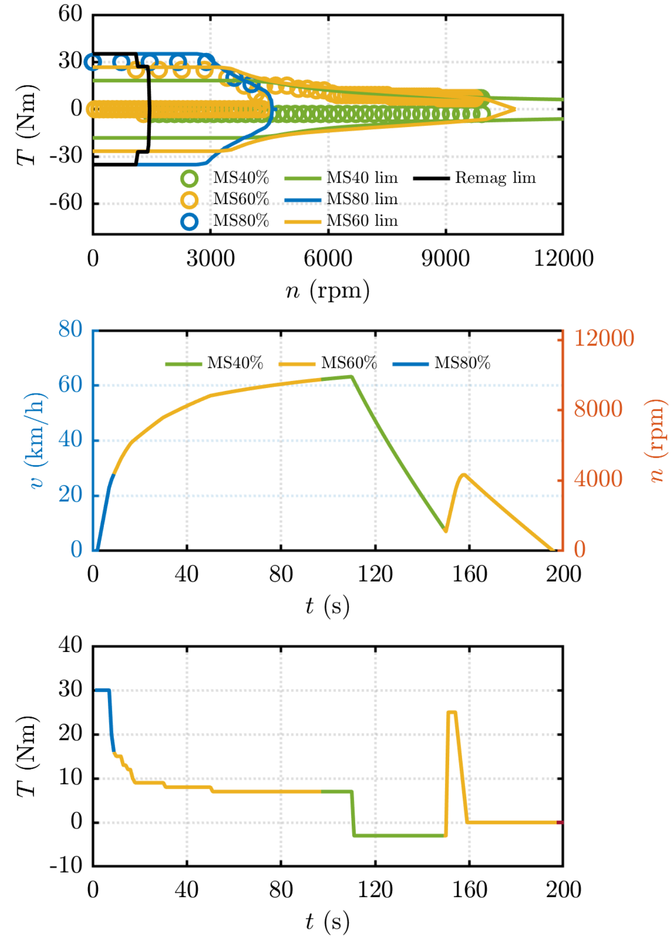

Fig. 10: Simple driving cycle test with MS switches between 40%, 60% and 80%.

B. Driving Cycle Test Results

The developed model is adopted for verifying the capability of the VFM drive to cover a driving cycle. For any required speed profile, the corresponding torque is computed based on the model of a full-size electric vehicle, with its parameters listed in Table II. A custom and a standard driving cycle (medium-low speed region of WLTC class 3) are adopted under two MS regulation strategies: the first one switching between 40% and 80% only, and the second one switching progressively between 40%, 60% and 80%. The results are illustrated in Figs. 9 to 12. Blue, yellow and green represent MS 80%, 60% and 40% operation, respectively; red indicates that the required torque exceeds the maximum $T-n$ envelop; black points are within the $T-n$ envelop but still unfeasible due to voltage limitations during re-magnetization.

TABLE II: Vehicle data

Vehicle total mass	1200 kg
Wheel diameter	0.406 m
Rolling resistance coefficient	0.02
Drag coefficient	0.5
Gear efficiency	0.97
Gear ratio	12

In the custom driving cycle illustrated in Fig. 9, the machine under test (MUT) is accelerated from 0 to 10000 rpm, decelerated to 1150 rpm, then accelerated again to 4300 rpm before coming to a stop. The MS is varied in discrete steps between 40% and 80% only. Initially, the vehicle operates at MS 80% and is demagnetized to 40% during acceleration beyond 4000 rpm, as the required torque exceeds the limit of the MS 80% torque–speed profile. The first deceleration phase is therefore carried out at MS 40%. At t=150 s, during the second acceleration phase, a torque demand of 25 Nm is imposed at a speed above 1150 rpm. This operating point lies outside the feasible torque–speed region for MS 40%, but would be achievable at MS 80%. However, since the speed never drops below the remagnetization voltage limit, a return to MS 80% is not possible. As a result, the required torque cannot be delivered, as indicated by the black points in Fig. 9. This demonstrates that the MUT is unable to complete the driving cycle due to the hysteresis effect imposed by the remagnetization voltage limit.

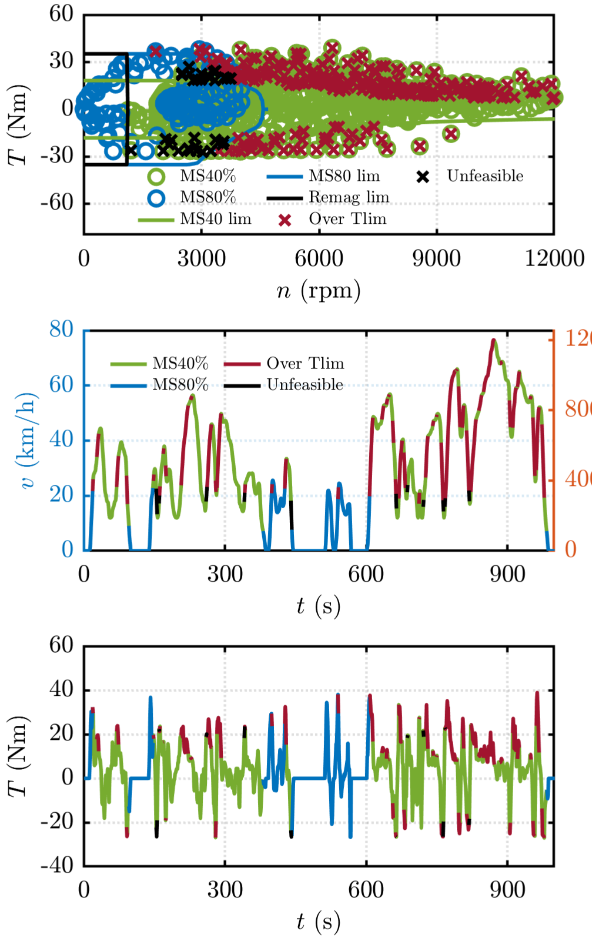

Fig. 11: WLTC driving cycle test with feasible and unfeasible operating points colored, MS switches between 40% and 80%.

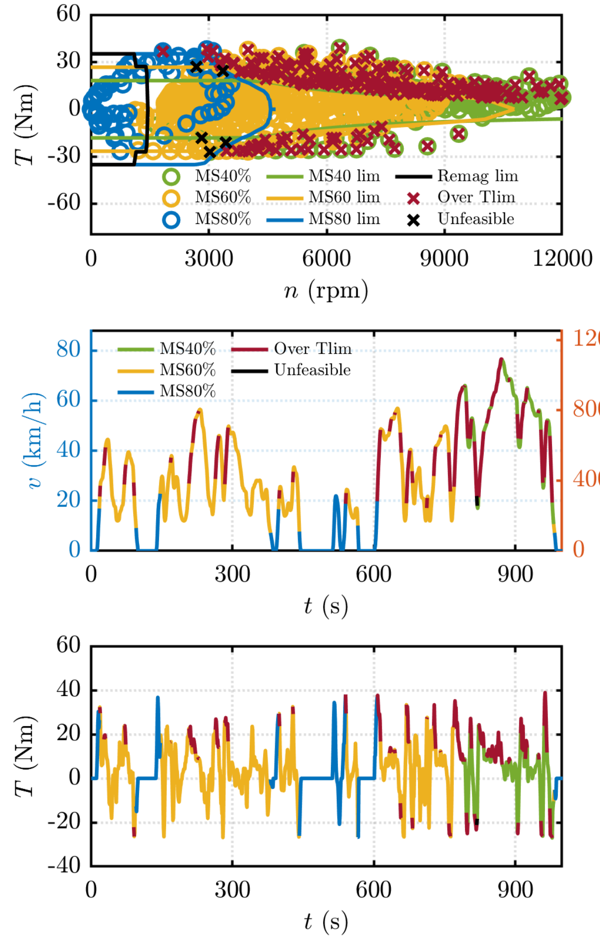

Fig. 12: WLTC driving cycle test with feasible and unfeasible operating points colored, MS switches between 40%, 60% and 80%.

The same driving cycle is analyzed in Fig. 10, this time with MS varied progressively through three levels: 40%, 60%, and 80%. The vehicle initially accelerates at MS 80%, then transitions to MS 60% at 4000 rpm, and finally to MS 40% at 9750 rpm. During the subsequent deceleration, the speed decreases to 1150 rpm, i.e. low enough to allow remagnetization to MS 60%. This intermediate MS level provides sufficient torque capability to meet the demands of the second acceleration phase. As a result, the finer granularity in MS adjustment mitigates the constraints imposed by the remagnetization voltage limit, enabling the MUT to successfully complete the driving cycle.

The same analysis is extended to the medium- and low-speed phases of the WLTC, as shown in Figs. 11 and 12, considering two and three MS levels, respectively. In this case, the MUT—being a downscaled prototype of a traction motor—is unable to complete the driving cycle. Operating points that fall outside the feasible T–n envelope are highlighted in red. Additionally, black markers indicate points that lie within the T–n envelope but remain unreachable due to voltage constraints during remagnetization. Although the MUT fails to meet the driving cycle requirements, the same methodology can be readily applied to full-scale VFMs to effectively assess their capability to fulfill specified driving profiles.

V. Conclusions

This paper analyzes the operational capabilities of VFMs, highlighting their ability to handle both low-speed, high-torque operation at high MS and field weakening at low MS. While the feasible operating area is typically represented as the envelope of maximum torque profile in the T–n plane, this study reveals that voltage constraints during remagnetization introduce a significant speed limitation. This results in hysteresis in MS regulation when speed varies.

To address this, the paper proposes a streamlined methodology for defining the VFM operating range that accounts for voltage limitations during remagnetization transients. This allows for rapid assessment of the feasibility of arbitrary load profiles. Furthermore, it is shown that employing finer steps in MS regulation can mitigate the associated torque penalties. The effectiveness of the proposed approach is validated through simulations on two driving cycles for a light vehicle, using different MS variation steps.

Acknowledgment

This publication is part of the project PNRR-NGEU which has received funding from the MUR-DM 352/2022 and Volvo Car Cooperation.

The research has been conducted with the support of Power Electronics Innovation Center (PEIC) of Politecnico di Torino.

References

[1] P. Ramesh and N. C. Lenin, "High power density electrical machines for electric vehicles—comprehensive review based on material technology," *IEEE Transactions on Magnetics*, vol. 55, no. 11, pp. 1–21, 2019.

[2] P. Pescetto, G. Dilevrano, F. Stella, G. Pellegrino, and A. Boglietti, "Enhanced short-time thermal transient model and testing procedure for high power density motors, such as in supercar traction," *IEEE Open Journal of Industry Applications*, vol. 6, pp. 391–402, 2025.

[3] A. Allca-Pekarovic, P. J. Kollmeyer, A. Forsyth, and A. Emadi, "Experimental characterization and modeling of a yasa p400 axial flux pm traction machine for performance analysis of a chevy bolt ev," *IEEE Transactions on Industry Applications*, vol. 60, no. 2, pp. 3108–3119, 2024.

[4] Z. Q. Zhu and D. Howe, "Electrical machines and drives for electric, hybrid, and fuel cell vehicles," *Proceedings of the IEEE*, vol. 95, no. 4, pp. 746–765, 2007.

[5] P. Pescetto, G. Dilevrano, G. Pellegrino, and A. Boglietti, "Lptn-based real-time stator hotspot temperature estimation for enhanced thermal management in high-performance pmsms," *IEEE Access*, vol. 13, pp. 103 166–103 177, 2025.

[6] I. Boldea, L. N. Tutelea, L. Parsa, and D. Dorrell, "Automotive electric propulsion systems with reduced or no permanent magnets: An overview," *IEEE Transactions on Industrial Electronics*, vol. 61, no. 10, pp. 5696–5711, 2014.

[7] H. Chen, J. Tang, Y. Liu, B. Jiang, and L. Boscaglia, "Electromagnetic performance investigation of a brushless electrically excited synchronous machine for long-distance heavy-duty electric vehicles," *IEEE Transactions on Transportation Electrification*, vol. 11, no. 1, pp. 225–235, 2025.

[8] A. Credo and P. Pescetto, "A systematic method for the calibration of fea model of synchronous reluctance machines considering manufacturing effects," *IEEE Open Journal of Industry Applications*, pp. 1–12, 2025.

[9] H. S. Badahdah and A. El-Refaie, "A review of recent topologies of variable flux machines," in *2024 International Conference on Electrical Machines (ICEM)*, 2024, pp. 1–7.

[10] V. Ostovic, "Memory motors," *IEEE Industry Applications Magazine*, vol. 9, no. 1, pp. 52–61, 2003.

[11] T. Fukushige, N. Limsuwan, T. Kato, K. Akatsu, and R. D. Lorenz, "Efficiency contours and loss minimization over a driving cycle of a variable flux-intensifying machine," *IEEE Transactions on Industry Applications*, vol. 51, no. 4, pp. 2984–2989, 2015.

[12] A. Athavale, K. Sasaki, B. S. Gagas, T. Kato, and R. D. Lorenz, "Variable flux permanent magnet synchronous machine (vf-pmsm) design methodologies to meet electric vehicle traction requirements with reduced losses," *IEEE Transactions on Industry Applications*, vol. 53, no. 5, pp. 4318–4326, 2017.

[13] R. Tu, H. Yang, H. Lin, H. Zhan, D. Wu, and M. Yu, "Design and optimization of a novel delta-type consequent-pole hybrid magnet memory machine," *IEEE Transactions on Energy Conversion*, vol. 39, no. 2, pp. 1265–1277, 2024.

[14] P. Peng and J. Zhang, "Design of a variable-flux permanent magnet machine using alnico 9 and comparison with a baseline interior permanent magnet machine," in *2019 IEEE Energy Conversion Congress and Exposition (ECCE)*, 2019, pp. 6524–6531.

[15] K. Yoneda, W. Suzuki, and K. Sakai, "Designing a leaf-benchmark variable magnetization-ipm motor with two v-shaped pms at a 100 kw power level," in *2022 IEEE Energy Conversion Congress and Exposition (ECCE)*, 2022, pp. 1–7.

[16] A. Athavale, D. J. Erato, and R. D. Lorenz, "Enabling driving cycle loss reduction in variable flux pmsms via closed-loop magnetization state control," *IEEE Transactions on Industry Applications*, vol. 54, no. 4, pp. 3350–3359, 2018.

[17] H. Yang, H. Lin, Z. Q. Zhu, D. Wang, S. Fang, and Y. Huang, "A variable-flux hybrid-pm switched-flux memory machine for ev/hev applications," *IEEE Transactions on Industry Applications*, vol. 52, no. 3, pp. 2203–2214, 2016.

[18] B. S. Gagas, K. Sasaki, T. Fukushige, A. Athavale, T. Kato, and R. D. Lorenz, "Analysis of magnetizing trajectories for variable flux pm synchronous machines considering voltage, high-speed capability, torque ripple, and time duration," *IEEE Transactions on Industry Applications*, vol. 52, no. 5, pp. 4029–4038, 2016.

[19] W. Liu, H. Yang, H. Lin, and S. Lyu, "Loss-reduction-oriented optimization methodology of hybrid-magnetic-circuit variable flux memory machine for global efficiency improvement," *IEEE Journal of Emerging and Selected Topics in Power Electronics*, vol. 10, no. 2, pp. 1658–1670, 2022.

[20] H. N. Phyu, Y. Zaifeng, A. Singh, and J. Hey, "Design and analysis of variable flux pm machine for extending speed region to improve the drive cycle efficiency," in *2024 27th International Conference on Electrical Machines and Systems (ICEMS)*, 2024, pp. 642–647.

[21] Y. Hu, B. Chen, Y. Xiao, X. Li, J. Chen, and H. Fang, "Comprehensive control of a hybrid-magnet variable-flux memory machine for washing machine applications," in *2021 IEEE 4th International Electrical and Energy Conference (CIEEC)*, 2021, pp. 1–6.

[22] K. Yuuki, K. Sakai, and H. Mochikawa, "Variable-flux motor drive system," US Patent 8 179 068, 2012.

[23] Y. Hu, B. Chen, Y. Xiao, X. Li, Z. Zhang, J. Shi, and L. Li, "Research and design on reducing the difficulty of magnetization of a hybrid permanent magnet memory motor," *IEEE Transactions on Energy Conversion*, vol. 35, no. 3, pp. 1421–1431, 2020.

[24] G. Weissitsch, T. Krainer, E. Marth, and G. Bramerdorfer, "Driving cycle based optimisation and comparison of variable flux permanent magnet machines," in *2024 IEEE Energy Conversion Congress and Exposition (ECCE)*, 2024, pp. 4923–4930.

[25] M. S. Mirazimi, C. Chen, P. Pescetto, S. Ferrari, G. Pellegrino, M. Diana, and T. Thiringer, "Accurate modeling of variable- flux pmsms without electromagnetic co-simulation," in *2024 International Symposium on Power Electronics, Electrical Drives, Automation and Motion (SPEEDAM)*, 2024, pp. 625–630.

[26] R. Garino, P. Pescetto, C. Chen, S. Ferrari, M. Diana, and G. Pellegrino, "Accurate simulation model of variable flux machines under asymmetrical demagnetization without fea co-simulation," in *2025 IEEE Energy Conversion Congress and Exposition (ECCE)*, 2025.